

Showcasing research from Reshef Tenne *et al.* at the Weizmann Institute of Science, Israel and co-workers at the Technische Universität Dresden, and the Ernst Ruska-Centre for Microscopy and Spectroscopy with Electrons and Peter Grünberg Institute, Germany.

Tubular structures from the LnS–TaS<sub>2</sub> (Ln = La, Ce, Nd, Ho, Er) and LaSe–TaSe<sub>2</sub> misfit layered compounds

Nanotubes from a new family of misfit compounds – LnX–TaX<sub>2</sub> (Ln = lanthanide atom; X = S, Se) are reported in this work. Careful structural study combined with computer simulations are used to characterize these new nanostructures.

As featured in:



See Reshef Tenne *et al.*,  
*J. Mater. Chem. C*, 2016, 4, 89.



[www.rsc.org/MaterialsC](http://www.rsc.org/MaterialsC)

Registered charity number: 207890

## PAPER

CrossMark  
click for updatesCite this: *J. Mater. Chem. C*, 2016,  
4, 89Tubular structures from the LnS–TaS<sub>2</sub> (Ln = La, Ce, Nd, Ho, Er) and LaSe–TaSe<sub>2</sub> misfit layered compounds†Gal Radovsky,<sup>a</sup> Ronit Popovitz-Biro,<sup>b</sup> Tommy Lorenz,<sup>c</sup> Jan-Ole Joswig,<sup>c</sup> Gotthard Seifert,<sup>c</sup> Lothar Houben,<sup>d</sup> Rafal E. Dunin-Borkowski<sup>d</sup> and Reshef Tenne<sup>\*a</sup>

Nanotubular structures from a new family of misfit compounds LnS–TaS<sub>2</sub> with (Ln = La, Ce, Nd, Ho, Er) and LaSe–TaSe<sub>2</sub> (some of them not known hitherto) are reported. Stress relaxation originating from the lattice mismatch between the alternating LnS(Se) and TaS<sub>2</sub>(Se) layers, combined with seaming of the dangling bonds in the rim, leads to the formation of a variety of nanotubular structures. Their structures are studied *via* scanning electron microscopy (SEM), high-resolution transmission electron microscopy (HRTEM), scanning transmission electron microscopy (STEM) and selected area electron diffraction (SAED). Tubules exhibiting a single folding vector for the LnS(Se) as well as TaS<sub>2</sub>(Se) layers were often found. The small values of the *c*-axis periodicities are indicative of a strong interaction between the two constituent layers which was also supported by Raman spectroscopy and theoretical calculations.

Received 18th September 2015,  
Accepted 22nd October 2015

DOI: 10.1039/c5tc02983j

www.rsc.org/MaterialsC

## Introduction

## Misfit layered compounds

Misfit layered compounds (MLC) have a general formula of (MX)<sub>1+y</sub>(TX<sub>2</sub>)<sub>m</sub> with (M = Sn, Pb, Sb, Bi, rare earths; T = Nb, Ta, Ti, V, Cr; X = S, Se; 0.08 ≤ *y* ≤ 0.28; *m* = 1–3).<sup>1,2</sup> The TX<sub>2</sub> and MX layers have different crystallographic structure and they are stacked periodically. TX<sub>2</sub> is a three-atom thick sandwich layer with a pseudo-hexagonal structure, in which the metal atoms are surrounded by six chalcogen atoms, either in octahedral or in trigonal prismatic coordination. Although bulk TaS<sub>2</sub> can adopt either structure,<sup>3–6</sup> trigonal prismatic is the relevant coordination in MLC.<sup>1,2,7</sup> The two atom thick MX slice can be considered as a distorted NaCl structure with an orthorhombic unit cell. The value of *y* is determined by the ratio of the projected atomic surface densities of the two subsystems. Interactions between the MX and TX<sub>2</sub> subsystems result in

various types of mutual structural modulations, depending on the compounds.<sup>1,2,7</sup> For the LnS–TaS<sub>2</sub> and LaSe–TaSe<sub>2</sub> MLC that are discussed here, the mutual structural modulation results in an in-plane commensurate “*b*” and an in-plane incommensurate “*a*” direction. In particular, the *b*-axis of LnS (Fig. 1a) fits to  $\sqrt{3} \times a$  of TaS<sub>2</sub>, where *a* is the in-plane lattice parameter of TaS<sub>2</sub> when indexed according to a pseudo-hexagonal unit cell (marked in brown in Fig. 1b). Therefore, it is convenient to describe the pseudo-hexagonal TaS<sub>2</sub> layer in terms of an ortho-pseudo-hexagonal unit cell that has primitive dimensions *a* and *b* =  $\sqrt{3} \times a$ , as shown in purple in Fig. 1b. A misfit then occurs along the *a* direction, as the ratio  $a_{\text{LnS}}/a_{\text{TaS}_2}$  is an irrational number. Therefore, the superstructure lacks three dimensional periodicity and it is impossible to define one common unit cell. A complete description of the entire structure is possible in a (3 + 1)*D* superspace<sup>1,2</sup> where an additional dimension (*D*) is inserted to reflect the incommensurate modulation of the atomic positions of the two subsystems along the *a*-axis.

It should be noticed that some of the compounds described in the present study, like HoS–TaS<sub>2</sub> and LaSe–TaSe<sub>2</sub>, were not reported in the literature before even in the bulk form.

Stability of LnS–TaS<sub>2</sub> misfit compounds

The Ln atoms within LnS–TaS<sub>2</sub> MLC inherently prefer a trivalent state.<sup>1,8</sup> It has been proposed that a considerable amount of charge transfer from LnS to the partially filled TaS<sub>2</sub> d<sub>22</sub> band<sup>8–10</sup> enhances the Coulombic interaction between the two sublayers which is believed to be one of the stabilizing mechanisms of these compounds. The d<sub>22</sub> band is a very narrow (~1 eV wide)

<sup>a</sup> Department of Materials and Interfaces, Weizmann Institute of Science, Rehovot 76100, Israel. E-mail: Reshef.Tenne@weizmann.ac.il; Fax: +972-8-934-4138; Tel: +972-8-934-2394

<sup>b</sup> Chemical Research Support, Weizmann Institute of Science, Rehovot 76100, Israel

<sup>c</sup> Physikalische Chemie, Technische Universität Dresden, Bergstr. 66b, D-01069 Dresden, Germany

<sup>d</sup> Ernst Ruska-Centre for Microscopy and Spectroscopy with Electrons and Peter Grünberg Institute, Forschungszentrum Jülich, D-52425 Jülich, Germany

† Electronic supplementary information (ESI) available: Structural aspects of the nanotubes, chemical analysis of the products, SEM images of the products, X-ray diffraction analysis of the product, tubular structures from LnS–TaS<sub>2</sub> (Ln = Ce, Nd, Ho) and LaSe–TaSe<sub>2</sub> MLC, literature values of interplanar spacings of TaS<sub>2</sub>(Se) and LnS(Se), theoretical calculations. See DOI: 10.1039/c5tc02983j

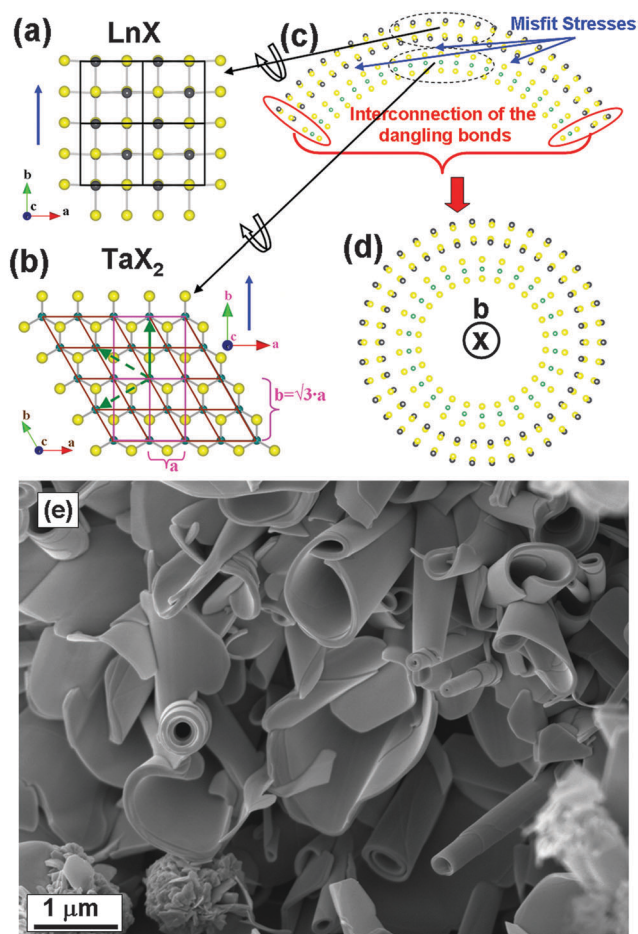


**Fig. 1** Schematic model showing the stacking and the relative in-plane orientation of the  $\text{TaX}_2$  and the  $\text{LnX}$  ( $X = \text{S}, \text{Se}$ ) layers in many of the tubular structures from the  $\text{LnX}-\text{TaX}_2$  MLC. (a) Single layer of  $\text{LnX}$  projected along the  $c$ -axis and oriented in such a way that its  $b$ -axis is parallel to the tubule axis (blue arrow) and to the solid green arrow in (b). (b) Single layer of  $\text{TaX}_2$  projected along the  $c$ -axis. Pseudo-hexagonal and ortho-pseudo-hexagonal unit cells are marked in brown and purple respectively. The solid green arrow represents the  $b$ -axis with respect to the ortho-pseudo-hexagonal unit cell, coincides with the tube axis (blue arrow). The two dashed green arrows represent crystallographically equivalent directions rotated by  $60^\circ$  and  $120^\circ$  relative to the direction marked by the solid green arrow. (c) Initiation of bending around the  $b$ -axes of the  $\text{LnX}$  and  $\text{TaX}_2$  layers that comprise an  $\text{LnX}-\text{TaX}_2$  slab. (d) A concentric tubule whose axis (perpendicular to the plane of the paper) coincides with the  $b$ -axes of  $\text{LnX}$  and  $\text{TaX}_2$ . (e) Representative partially unfolded sheets, demonstrating the scrolling process for the  $\text{NdS}-\text{TaS}_2$  MLC case in particular.

band formed by the hybridization of  $d_{z^2}$  and  $d_{x^2-y^2}$  Ta orbitals and is half full in  $2\text{H}-\text{TaS}_2$ .<sup>8-10</sup>

The larger amount of charge transfer may result in higher Coulombic interaction between the  $\text{LnS}$  and the  $\text{TaS}_2$  layers, shorter bond lengths between the Ln and the S atoms of the  $\text{TaS}_2$  layer<sup>8</sup> and smaller periodicity values along the  $c$ -axis.

### Magnetic and electrical properties of the bulk materials

As a result of the magnetic moment of the two atom thick  $\text{LnS}$  layers, bulk  $\text{LnS}-\text{TaS}_2$  MLC have been found to exhibit interesting magnetic properties.<sup>1,10</sup> For example, it was shown

that when  $\text{Ln} = \text{Ce}, \text{Gd}$  and  $\text{Dy}$  the magnetic susceptibility shows a maximum at 2.7, 4.1 and 1.7 K, respectively. This observation was attributed to low temperature antiferromagnetic ordering.<sup>10</sup> However, when  $\text{Ln} = \text{Nd}, \text{Er}$ , the susceptibility obeyed the Curie-Weiss law and showed no magnetic transition down to 1.2 K (the lowest temperature investigated in these studies).<sup>10</sup>  $\text{LaS}-\text{TaS}_2$  has been found to be diamagnetic.<sup>10</sup> Bulk  $\text{LnS}-\text{TaS}_2$  MLC have a metallic temperature dependence of their electrical conduction.<sup>1,8,10</sup> However, in contrast to  $\text{MS}-\text{TaS}_2$  (with  $M = \text{Sn}, \text{Pb}, \text{Bi}, \text{Sb}$ )<sup>11,12</sup> MLC, no superconducting transitions have been reported for these compounds.

Nanotubes from the  $\text{LnS}-\text{TaS}_2$  MLC exhibit unique structural characteristics not described hitherto, and potentially have interesting magnetic and electrical properties. However, magnetic and electrical measurements are time consuming and will be the scope of future publications.

### Formation of tubular structures

The misfit in the  $a$ - $b$  plane is the main driving force for scrolling as shown in Fig. 1c. In the MLC discussed here, such a misfit occurs along the  $a$ -axis. The tubule axis is then expected to be parallel to the common  $b$ -axis and perpendicular to the  $a$ -axis along which the lattice parameters differ most as shown in Fig. 1a.

Upon scrolling, the energy associated with the misfit is reduced.<sup>13</sup> Spontaneous bending is mostly expected for an asymmetric  $\text{MX}-\text{TX}_2$  lamella, *i.e.* one that is bounded by  $\text{MX}$  on one side and by  $\text{TX}_2$  on the opposite side. The formation of the nanotubes is further stimulated by the seaming of dangling bonds at the rims of the layers as reported before for binary layered compounds, like  $\text{WS}_2$ , and is shown schematically in Fig. 1c. These two independent mechanisms promote the formation of concentric tubules which may effectively decrease the minimal equilibrium radius resulting from the misfit.

## Experimental and computational section

### Synthesis of the tubular structures

The synthesis of  $\text{LnS}-\text{TaS}_2$  ( $\text{Ln} = \text{La}, \text{Ce}, \text{Nd}, \text{Ho}, \text{Er}$ ) and  $\text{LaSe}-\text{TaSe}_2$  MLC tubular structures was carried out in evacuated ampoules at a vacuum of  $\sim 5 \times 10^{-5}$  torr. Ta, Ln, S or Se powders were taken at molar ratios of  $\sim 1 : 1 : 3$ . Small amounts of  $\text{TaCl}_5$  or  $\text{TaBr}_5$  ( $\sim 0.1$  of a molar amount of Ta) powder were added as a Cl/Br source. Cl/Br is believed to act as a transport agent. The powders used were purchased from the following companies and had the following purity: La, Ho, Er (Strem Chemicals 99.9%), Nd (Strem Chemicals 99.8%), Ce (Alfa Aesar 99.9%), Ta (Alfa Aesar 99.9%), S (Sigma Aldrich 99.98%), Se (Fluka 99.9%),  $\text{TaCl}_5$  (Alfa Aesar 99.8%),  $\text{TaBr}_5$  (Strem Chemicals 99.9%). The materials were inserted into the ampoule in a glove box at a nitrogen atmosphere to prevent oxidation. After sealing, the ampoules were inserted into a preheated vertical furnace and two annealing steps were performed. First, the ampoules were held in a temperature gradient of  $400^\circ\text{C}$  at the bottom (with the precursors) and  $850^\circ\text{C}$  at the upper part for 1 h. In the second

step, the temperatures were tuned to 850 °C at the bottom (with the precursors) and 50 °C at the upper part. This step lasted for 4–16 h. Afterwards the ampoules were removed rapidly from the furnace and were cooled at plain air. Most of the product remained at the hot edge of the ampoules and the amount of the substance transported to the cold edge was negligible. It should be emphasized that the nanotubes are obtained in appreciable yields under a narrow window of conditions, only. Otherwise, micron-size platelets of the same compounds or the binary compounds predominate in the reaction product.

### Electron microscopy, XRD, Raman spectroscopy

After the ampoules were opened, the powder products from the hot zone were examined by SEM, HRTEM, STEM, XRD, and Raman spectroscopy.

X-ray diffraction (XRD) patterns were recorded with a Rigaku TTRAXIII diffractometer (Cu-K $\alpha$  radiation, 1.54 Å) operating in the Bragg–Brentano ( $\theta$ – $2\theta$ ) mode. For SEM analysis, a small amount of the powder was placed on carbon tape stuck to an aluminum stub. The resulting samples were examined using a Zeiss Ultra model V55 SEM and a LEO model Supra 55VP SEM equipped with an EDS detector (Oxford model INCA).

For high-resolution transmission electron microscopy (HRTEM) a solution of the product in ethanol was dripped onto a lacey/holey carbon/collodion-coated Cu grids. The resulting samples were examined by Philips CM120 TEM, operating at 120 kV equipped with EDS detector (EDAX-Phoenix Microanalyzer); JEOL JEM2100 operating at 200 kV and FEI Tecnai F30-UT HRTEM operating at 300 kV. High-resolution scanning transmission electron microscopy (STEM) images and EDS chemical maps were taken on a probe-corrected FEI Titan 80-200 G2 ChemiSTEM instrument equipped with a Bruker Super-X detector at 200 kV.

For Raman spectroscopy measurements, droplets of an ethanol solution containing the product were dripped on Si wafers. Raman measurements were carried out using a Renishaw Micro Raman InVia Imaging Microscope equipped with a CCD device. Tubes with diameters of 0.2–1  $\mu\text{m}$  could easily be discerned using the light microscope. A He–Ne laser ( $\lambda = 633 \text{ nm}$ ) was used for excitation.

### Computational details

The present calculations were based on the density-functional tight-binding (DFTB) method. For these calculations, rectangular periodic boundary conditions were applied. The effective one-electron potential in the Kohn–Sham Hamiltonian is approximated as a superposition of the potentials of the neutral atoms. Furthermore, only one- and two-center integrals are calculated to set-up a scalar relativistic Hamilton matrix. The valence basis included the 6s, 6p, and 5d orbitals for La; 3s and 3p orbitals for S and the 5s, 5p, and 4d orbitals for Ta. The states below these levels were treated within a frozen-core approximation. For a detailed description of the calculations, see Section S7.1 in the ESI.†

## Results and discussion

Here nanotubes from a new family of LnS–TaS<sub>2</sub> (LaSe–TaSe<sub>2</sub>) MLC, are reported. The tubular phase constituted ~50% of the total product for the LaS–TaS<sub>2</sub> case, ~20% for NdS–TaS<sub>2</sub> and ErS–TaS<sub>2</sub>, ~5% for HoS–TaS<sub>2</sub> and LaSe–TaSe<sub>2</sub> and merely 1% for the CeS–TaS<sub>2</sub> case. Syntheses were carried out in fused silica tubes under vacuum. The tubular structures were produced in the hot zone of the ampoules among other by-products, in contrast to *e.g.* MS–TaS<sub>2</sub> with M = Sn, Pb, Bi, Sb that condensed at the cold end of a temperature gradient.<sup>7</sup> The addition of a small amount of TaCl<sub>5</sub> or TaBr<sub>5</sub> powders was essential for nanotube growth. The use of TaBr<sub>5</sub> instead of TaCl<sub>5</sub> resulted in a higher yield in the case of LaSe–TaSe<sub>2</sub> nanotubes. For the sake of comparison, iodine was used as a transport agent for the growth of LnS–TaS<sub>2</sub> MLC single crystals which were obtained at the cold zone of the tube within several days. Also, the ampoules were subjected to a very fine temperature gradient of 850–950 °C between the edges.<sup>10</sup> Typically, a deviation of only a few degrees from the prescribed procedure leads to an appreciably smaller yield of the nanotubes in the product.

Chemical analysis of the LnS–TaS<sub>2</sub> with (Ln = La, Ce, Nd) tubular structures using both EDS within the SEM and TEM (of individual nanotubes) indicated the presence of 1–2 at% of Cl or Br in the case of LaSe–TaSe<sub>2</sub>. Indeed, peaks of Cl (Br) are clearly seen on the EDS spectra recorded from these compounds as shown in Fig. S2 in the ESI.† However, no clear peak of Cl could be detected for (Ln = Ho and Er). Nevertheless, in all cases (of LnS–TaS<sub>2</sub> with Ln = La, Ce, Nd, Ho, Er and LaSe–TaSe<sub>2</sub>) tubular structures could not be produced without the addition of TaCl<sub>5</sub> (TaBr<sub>5</sub>) powder to the ampoules.

Representative SEM images of the products are shown in Fig. 2 and Fig. S3 in the ESI.†

Table 1 summarizes the typical range of outer diameters of the tubules as well as their yields of production.

The ratio between the inner and outer diameters varied between the limiting cases of 0 and 1 for all of the LnS(Se)–TaS<sub>2</sub>(Se) MLC tubular structures that are described here. Partially unrolled LnS–TaS<sub>2</sub> MLC sheets, as well as pristine TaS<sub>2</sub>, LnS, and metallic Ln and Ta residuals (identified from XRD spectra; see Fig. 5 and Section S4 in the ESI†) were always present in the powder. It is suggested that in several cases after the initial tube is produced, further layers can form within the preformed core which serves as an “internal template”. Presumably also, the growth of the nanotubes did not start at once with some nanotubes starting to grow earlier and others later-on. Hence some of the nanotubes stayed longer in the reaction zone giving rise to the possibility for a secondary growth (templating effect) on the outer as well as the inner-most surface layer of the nanotube. Therefore, nanotubes of different internal and external diameters and length were obtained. That might explain the large variety of the internal diameters within the tubes. Furthermore, the seaming of the dangling bonds provides additional driving force for the formation of concentric tubes with small internal diameter. Energy-wise, templated growth is not as demanding and may lead to scrolling, as is often observed

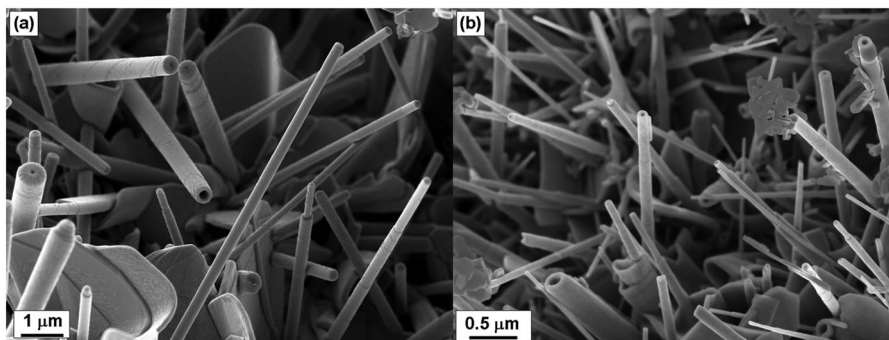


Fig. 2 SEM images of the tubular structures and common by-products from (a) LaS–TaS<sub>2</sub>, (b) ErS–TaS<sub>2</sub> MLC. Scrolling steps are visible at the significant part of the tubular crystals.

Table 1 Typical range of outer diameters of the LnS(Se)–TaS<sub>2</sub>(Se) tubular structures and their yield of production

Compound	Yield [%]	Outer diameter [nm]
LaS–TaS <sub>2</sub>	50	40–1000
CeS–TaS <sub>2</sub>	1	60–1000
NdS–TaS <sub>2</sub>	20	130–1200
HoS–TaS <sub>2</sub>	5	45–300
ErS–TaS <sub>2</sub>	20	35–300
LaSe–TaSe <sub>2</sub>	5	85–1000

for the outermost layers of the tubular structures. Therefore, in such cases part of the layers have a tube-like morphology and part (mostly the outermost layers) show a scroll like structure.

## Structural analysis of the tubular structures

In many of the tubules from all of the LnS(Se)–TaS<sub>2</sub>(Se) MLC that are discussed here, the classical behavior of one common *b*-axis coinciding with the tubule axis (as presented in Fig. 1) was observed. In this case both the TaS<sub>2</sub>(Se) and the LnS(Se) layers had a single folding vector. Tubules exhibiting two folding vectors of the TaS<sub>2</sub> layers with one two or three folding vectors of the LnS layers were encountered as well (see Section S1.1 in the ESI<sup>†</sup>). The latter configuration of the layers is very common in nanotubes from the PbS–NbS<sub>2</sub><sup>14</sup> and PbS–TaS<sub>2</sub><sup>7</sup> MLC which were widely described by us in the past.

TEM images of LnS–TaS<sub>2</sub> with (Ln = La, Ce, Nd, Ho, Er) and LaSe<sub>2</sub>–TaSe<sub>2</sub> tubular structures are shown in Fig. 3 and Fig. S5–S8 in the ESI.<sup>†</sup> The SAED patterns of the shown tubular structures indicate that there is a single folding vector for both the TaS<sub>2</sub>(Se) and the LnS(Se) layers, consistent with the structure shown in Fig. 1d. Such patterns were commonly encountered for LnS–TaS<sub>2</sub> (Ln = La, Er) as shown in Fig. 3a and b and more rarely for (Ln = Ce, Nd, Ho) and LaSe–TaSe<sub>2</sub> as shown in Fig. S7a, S6a, S6b and S5, respectively, in the ESI.<sup>†</sup> Fig. 3a shows the structure of a LaS–TaS<sub>2</sub> nanotube. Here, the LaS and TaS<sub>2</sub> layers are stacked in an alternating sequence along their common *c*-axis with a 1.15 nm periodicity, as determined from line profiles and from the distance between

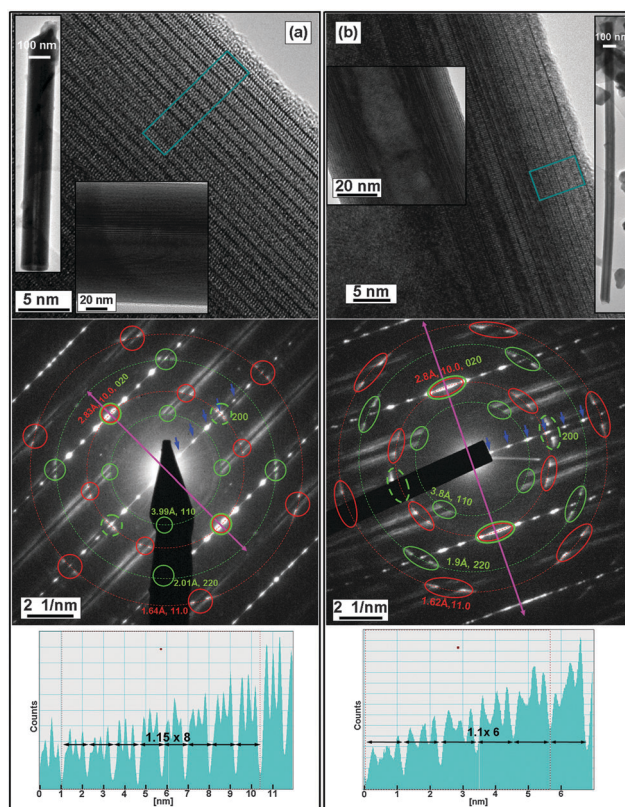


Fig. 3 TEM images of (a) LaS–TaS<sub>2</sub> and (b) ErS–TaS<sub>2</sub> tubular crystals, with the LnS and TaS<sub>2</sub> layers stacked periodically. Top: High magnification images, with medium and low magnification images shown as insets. Middle: SAED patterns acquired from the areas shown in the upper images. Spots corresponding to the same interplanar spacings are marked by large segmented ellipses or circles (red for TaS<sub>2</sub> and green for LnS) and the respective Miller indices are indicated. The tubule axes are marked by purple double arrows. Basal reflections are marked by small blue arrows. Chiral angles of 3.1° and 7.2° for the tubules shown in (a) and (b), respectively, were determined from the splitting of the spots, as discussed in the text. Bottom: Line profiles perpendicular to the tubule axes integrated along the rectangles marked in the upper images.

basal reflections in diffraction patterns. In Fig. 3a, six pairs of spots with interplanar spacings of 1.64 Å and 2.83 Å are equally-azimuthally distributed on a circle and are marked by small red

circles. These spots are attributed to the (11.0) and (10.0) planes of TaS<sub>2</sub> ((200) and (020) in the ortho-pseudo-hexagonal indexing system). The multiplicity factor for these planes is six.<sup>6</sup> This observation suggests the presence of a single folding vector for the TaS<sub>2</sub> layers. Four pairs of spots belonging to the LaS sublattice with interplanar spacings of 3.99 Å and 2.01 Å are marked by small green circles and attributed to the (110) and second order (220) reflections. The multiplicity factor for these planes is four,<sup>15</sup> indicating that there is also a single folding vector for the LaS layers in this tube. The splitting of the  $hk.0$  (of TaS<sub>2</sub>(Se)) and  $hk0$  (of LnS(Se)) diffraction spots indicates a small chiral angle for both of the layers (see Section S1.2 in the ESI†). In the tubules analyzed here, the chiral angles of the TaS<sub>2</sub>(Se) and LnS(Se) within the same tubule are equal along the entire length of the nanotube, which attests to its crystalline quality. The values of the chiral angles are indicated in the figure captions.

Two pairs of LaS 020 spots match the 10.0 spots of TaS<sub>2</sub> (020 when indexed in the ortho-pseudo-hexagonal system) parallel to the tubule axis. These coincident spots (marked with both green and red small circles) reveal the presence of a common commensurate in-plane direction  $b$  that coincides with the nanotube axis, as expected and as shown in Fig. 1d. 200 LaS spots also appear and are marked by segmented small circles. As expected, these spots appear at azimuthal angles of 90° with respect to the 020 spots, which is equal to the angle between the (200) and (020) planes in orthorhombic LaS. The fact that the LaS 200 spots are approximately on the same circle as the 020 spots indicates that the  $a$  and  $b$  lattice parameters of LaS are almost equal. The first order LaS 010 and 100 spots are absent from the pattern, in agreement with previous observations.<sup>7,14</sup>

The SAED patterns of the LnS-TaS<sub>2</sub> (Ln = Ce, Nd, Ho, Er) and LaSe-TaSe<sub>2</sub>, which are shown in Fig. S5, S6a, b, S7a (ESI†) and Fig. 3b, are similar to the pattern shown in Fig. 3a. However, the lattice periodicities of the latter MLC nanotubes are different from those of their LaS-TaS<sub>2</sub> counterpart (see Table 2 and Section S5 in the ESI†). For example, in the ErS-TaS<sub>2</sub> tubule shown in Fig. 3b, it is apparent that the 200 spots of ErS (marked by segmented green ellipses) are “shifted” slightly away from the red dashed circles that correspond to the 10.0 spots of TaS<sub>2</sub> and the 020 spots of ErS. This shift is indicative of the presence of a slightly smaller interplanar  $a$ -spacing, when compared to the  $b$ -spacing of the ErS layer. Therefore, in this

case the difference between the in-plane lattice parameters ( $a$  and  $b$ ) of LnS (*i.e.*, ErS) is more apparent. Such a shift is also apparent for HoS-TaS<sub>2</sub> tubular structures (Fig. S6b, ESI†), but not for LaS-TaS<sub>2</sub> (Fig. 3a), CeS-TaS<sub>2</sub> (Fig. S7a, ESI†), NdS-TaS<sub>2</sub> (Fig. S6a, ESI†) or LaSe-TaSe<sub>2</sub> (Fig. S5, ESI†). Also, for the LaSe-TaSe<sub>2</sub> tubule shown in Fig. S5 (ESI†), the lattice periodicities are significantly larger than for the LaS-TaS<sub>2</sub> counterpart.

The in-plane lattice parameters ( $a$  and  $b$ ) of LnS and TaS<sub>2</sub> (labeled according to the ortho-pseudo-hexagonal system) were calculated from the 10.0 and 11.0 reflections of TaS<sub>2</sub>(Se) and from the 220 reflections of LnS(Se). The  $b$ -axis is commensurate and common to both the LnS and the TaS<sub>2</sub> and was assumed to be equal for the calculations. The results are summarized in Table 2. The average stoichiometry of the tubes' constituents could be extracted from the lattice parameters of the TaS<sub>2</sub>(Se) and the LnS(Se) layers deduced from the SAED patterns. The approximate stoichiometries could be calculated from the ratio of the projected atomic surface densities of the two sublayers. The value of  $y$  within the LnS<sub>1+y</sub>TaS<sub>2</sub> (or Se counterparts) can be calculated according to  $2(a_{\text{TaS}_2}/a_{\text{LnS}}) - 1$  where the factor 2 represents the ratio of the number of formula units in the unit cell of each sublattice (4 for LnS(Se) and 2 for TaS<sub>2</sub>(Se)). These results are summarized in Table 2 as well and are comparable to the bulk MLC counterparts. However, it is important to note that the exact stoichiometry of each LnS-TaS<sub>2</sub> couple of layers within the multilayer tube must be slightly different due to the different projected perimeters of the layers (and consequently the size of the sheet) required to bend and seam the tubes into slightly different diameters.

Direct structure images of LnS-TaS<sub>2</sub> nanotubes, carried out in a Titan 80-200 G2, are consistent with the results of the analysis of the SAED patterns. Fig. 4 shows representative high-resolution STEM images of a LaS-TaS<sub>2</sub> nanotube. The high-angle-scattered intensity is stronger for the TaS<sub>2</sub> layers owing to their greater projected cation density. Therefore, the TaS<sub>2</sub> layers appear brighter in high-angle annular dark field (HAADF) images and dark in bright-field (BF) STEM images. A perfectly alternating sequence of layers with a single folding vector is observed for all LaS-TaS<sub>2</sub> periods of the nanotube shell. The structure overlay in Fig. 4b shows that the folding of the tube is along the incommensurate  $a$ -axis, while the tube axis is parallel to the commensurate  $b$ -axis, as shown in Fig. 1d. Notwithstanding the fact that Fig. 4 was taken with full atomic resolution, the

**Table 2** Typically measured interplanar spacings in tubular structures from LnS(Se)-TaS<sub>2</sub>(Se) MLC. \*For TaS<sub>2</sub>(Se), (11.0) and (10.0) planes labeled in the pseudo-hexagonal system are equivalent to (200) and (020) planes, respectively, in the ortho-pseudo-hexagonal system. In-plane ( $hk0$ ) spacings were deduced from SAED solely, while the  $c$ -axis periodicities of the superstructures were deduced from SAED and XRD patterns as well in several cases

Compound	TaS <sub>2</sub> $d(11.0) = d(200)^* = a/2$ [Å]	TaS <sub>2</sub> $d(10.0) = d(020)^* = b/2$ [Å]	LnS(110) [Å]	LnS(220) [Å]	LnS(200) = $a/2$ [Å]	LnS(020) = $b/2$ [Å]	Difference between $a$ and $b$ of LnS [%]	Mean $c$ -axis periodicity ED/XRD [Å]	The value of $y$ within (LnS) <sub>1+y</sub> TaS <sub>2</sub>
LaS-TaS <sub>2</sub>	1.64	2.83	3.99	2.01	2.86	2.83	1	11.5/11.45	0.145
CeS-TaS <sub>2</sub>	1.64	2.84	4.00	2.01	2.845	2.84	0.17	11.45	0.15
NdS-TaS <sub>2</sub>	1.63	2.82	3.86	1.98	2.78	2.82	1.4	11.4/11.28	0.17
HoS-TaS <sub>2</sub>	1.61	2.8	3.8	1.91	2.61	2.8	7.3	11.1	0.23
ErS-TaS <sub>2</sub>	1.62	2.8	3.8	1.9	2.59	2.8	8	11.1/11.11	0.25
LaSe-TaSe <sub>2</sub>	1.71	2.98	4.22	2.12	3.02	2.98	1.2	12	0.13

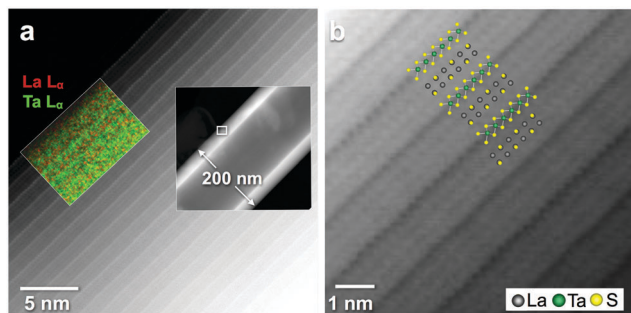


Fig. 4 High-resolution STEM images of a LaS–TaS<sub>2</sub> nanotube. (a) HAADF image. The insets show an HAADF image corresponding to a larger field of view, with a marker indicating the magnified region, and a high-resolution chemical map acquired by EDS. (b) Atomic-resolution BF STEM image, with structure projections of the LaS and TaS<sub>2</sub> layers superimposed.

intrinsic tubular structure imposed a severe restriction on the visibility of sulfur. In fact, the tantalum and lanthanum atoms overlap with sulfur in projection owing to the bending of the nanotube shells and hence the sulfur signal is not detected against the background of the heavy atom signal. Consequently, no effort was undertaken for structure refinement in this analysis.

Stacking disorder of the LnS (with Ln = La, Ce, Nd, Ho, Er) and TaS<sub>2</sub> layers along the *c*-axis was also observed, as shown for a NdS–TaS<sub>2</sub> MLC in Fig. S8 in the ESI.† As a result, the basal reflections (marked by a blue bracket in Fig. S8c, ESI†) are smeared. Also, part of the Ta–Ce–S tubules were found to exhibit a periodicity of 2.43 nm along the *c*-axis, as shown in Fig. S7b in the ESI.† This periodicity is more than twice the regular periodicity of 1.145 nm, which corresponds to the CeS/TaS<sub>2</sub> (1:1) periodic stacking. The structure of these Ta–Ce–S nanotubes could not be fully interpreted at this point.

X-ray diffraction (XRD) patterns recorded from the total products obtained during the attempts to synthesize LaS–TaS<sub>2</sub>, NdS–TaS<sub>2</sub> and ErS–TaS<sub>2</sub> tubular structures are shown in Fig. 5 and Fig. S4 in the ESI.† A series of different diffraction orders 00*n* (basal reflections similar to the reflections marked by small blue arrows in the SAED patterns), corresponding to the LnS–TaS<sub>2</sub> MLC (superstructures) with LnS and TaS<sub>2</sub> layers stacked periodically along the *c*-axis, can be clearly identified. For the 001 (first order) superstructure peaks, corresponding values of 11.45 Å, 11.28 Å and 11.11 Å were obtained for LaS–TaS<sub>2</sub>, NdS–TaS<sub>2</sub> and ErS–TaS<sub>2</sub> MLC, respectively. The line profiles generated from (HRTEM) images yielded quite similar values of 11.5 Å, 11.4 Å and 11.1 Å.

Other XRD peaks were assigned to the non-basal reflections arising from the structurally modulated LnS and TaS<sub>2</sub> layers. The (110), (100) planes of TaS<sub>2</sub> (or 200 and 020 respectively according to the ortho-pseudohexagonal system of labeling) as well as (110) and (220) planes of LnS within the LnS–TaS<sub>2</sub> MLC are marked on the patterns (the 020 peaks of LnS coincide and 200 roughly coincide with that of 10.0 of TaS<sub>2</sub>). These diffraction peaks correspond to the SAED peaks marked by the red and green markers respectively in Fig. 3a, b and Fig. S6a in the ESI.†

It is known from the literature<sup>1,2,16</sup> that for most of the MLC in their planar form a shift of *b*/2 along the *b*-axis between two

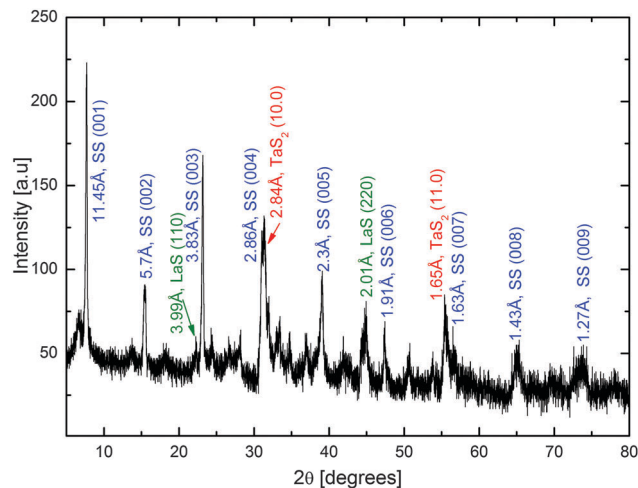


Fig. 5 Representative XRD pattern recorded from the total product obtained during the synthesis of LaS–TaS<sub>2</sub> tubular structures. Different orders of peaks associated with the LnS/TaS<sub>2</sub> (1:1) superstructure (SS) along the common *c*-axis are marked in blue. The corresponding interplanar spacings are also marked.

consequent layers of the same type is observed leading by that to a “doubling” of the periodicity along the stacking direction for that specific subsystem. The stacking is named C-centered when its periodicity is 11–12 Å (with no *b*/2 shift) and F-centered when the periodicity is twice that distance, *i.e.* 22–24 Å (*i.e.* including the *b*/2 shift). These configurations were actually determined from the intensity-ratio of the TX<sub>2</sub> and the MX peaks of the XRD patterns (in some cases with the assistance of SAED patterns of planar sheets).<sup>1,16</sup> It is possible that the periodicity of one of the subsystems, *e.g.* TX<sub>2</sub> would be twofold of MX or *vice versa*. (Four possibilities are possible CC, CF, FC and FF, the first letter corresponds to MX and the second to TX<sub>2</sub>)<sup>1,2,16</sup> However, in the tubular structures described above the situation is even more complex. The successive layers of the same type might also be slightly shifted one with respect to the other due to the folding of each layer into a tube of a slightly different diameter. As stated earlier, many tubes reported here possess a single folding vector of the LnS(Se) and the TaS<sub>2</sub>(Se) layers with one common *b*-axis coinciding with the tubule axis. However, a fraction of the analyzed LnS(Se)–TaS<sub>2</sub>(Se) nanotubes exhibited different rotational variants of the LnS(Se) and the TaS<sub>2</sub>(Se) layers with two different mutual orientations (between the LnS(Se) and TaS<sub>2</sub>(Se)) and orientations relative to the tubule axis as detailed in Section S1.1 in the ESI.† This situation is completely analogous to the case of the PbS–TaS<sub>2</sub><sup>7</sup> and PbS–NbS<sub>2</sub><sup>14</sup> nanotubes described before. Therefore the consequent layers of the same type are not only “shifted” but also rotated one relative to the other. Since XRD is obtained from the whole product the ratios of the peak’s intensities can not be directly related with the type of centering (the *b*/2 movement of the consequent layers of the same type related to planar crystals). Also, it was shown previously from SAED data that the *b*/2 shifts deduced from XRD are not a general feature and often occur non-systematically even for planar crystallites.<sup>16</sup>

It is well established that, in contrast to planar crystals, the Bragg conditions for diffractions from the basal as well as from

non-basal planes can be potentially fulfilled simultaneously within the same tubule (for different incidence  $\theta$  angles). For a tubule lying on a plane surface (parallel to the sample plane) the basal (XRD) reflections are obtained from the upper and the bottom part of the tubule. However the diffraction from the  $hk0$  planes of LnS and the TaS<sub>2</sub> are obtained from the side walls of the tubule. Therefore, in the case of nanotubes, diffraction peaks can be produced from both, for the correct incident angles according to the Bragg's law. Therefore the difference between the intensities of the basal and the non basal reflections cannot be attributed to preferred orientation (texture). XRD patterns representing texture are well documented in the literature for the case of planar (non-tubular) crystallites (see p. 14 in ref. 1).

Peaks arising from the residual by-products, such as pristine LnS (Ln = La, Nd, Er), (and also 1T-TaS<sub>2</sub> in Fig. S4a and b, ESI†) and excess unreacted metallic Ln or Ta were also observed however for simplicity reasons they are not marked in the XRD patterns.

The  $00n$  XRD peaks are rather broad (full width at half maximum  $\sim 0.3$  Å for the 001 first order reflection). This suggests the presence of a statistical distribution for the interlayer spacing along the  $c$ -axis of the LnS/TaS<sub>2</sub> (1 : 1) superstructure. This observation was also confirmed by statistical analysis of electron diffraction data. Furthermore, a spreading of  $\sim 3\%$  in the (10.0) and (11.0) in-plane interplanar spacing for TaS<sub>2</sub> and (110) and (220) in-plane interplanar spacing for LnS was observed in the analysis of the SAED patterns recorded from multiple (20–30) tubes. For every compound, average values for the mentioned spacings were calculated and tubules fitting these values were chosen for presentation. The mentioned spreading of 3% refers to the maximum difference between the upper and the lower measured values of the mentioned interplanar spacings for every compound individually.

The values of the interplanar spacing obtained from the SAED/XRD patterns are comparable to published values for the bulk MLC materials (see Table S1, ESI†). No XRD patterns were recorded from CeS-TaS<sub>2</sub>, HoS-TaS<sub>2</sub> or LaSe-TaSe<sub>2</sub> due to the low yield of nanotubes in the products. In these compounds, the periodicity was determined solely from SAED patterns, as summarized in Table 2.

All the LnS compounds that are discussed here are stable in bulk form, with NaCl crystal structures and space group  $Fm\bar{3}m$ . However, as a result of the mutual structural modulation that occurs in MLC, the structures of bilayers are distorted slightly when compared to the pristine bulk phase. The interplanar spacings of TaS<sub>2</sub> and LnS (with Ln = La, Ce, Nd, Er) within bulk LnS-TaS<sub>2</sub> MLC, as well as their values in pristine bulk form, are given in Table S1 in the ESI.† To the best of our knowledge, bulk HoS-TaS<sub>2</sub> and LaSe-TaSe<sub>2</sub> MLC have not been reported previously. Therefore, in these cases only values for bulk HoS, LaSe, TaS<sub>2</sub> and TaSe<sub>2</sub> are given in this table.

The in-plane and  $c$ -axis lattice constants of tubular structures of the LnS-TaS<sub>2</sub> MLC are smaller than those of their MS-TaS<sub>2</sub> (M = Sn, Pb) counterparts. Since the Ln atoms prefer a trivalent state, while Pb and Sn are divalent, charge transfer from the LnS layers to the TaS<sub>2</sub> layers is expected to be greater than for PbS or SnS.<sup>7,8,10</sup> BiS-TaS<sub>2</sub> and SbS-TaS<sub>2</sub> can be considered as an

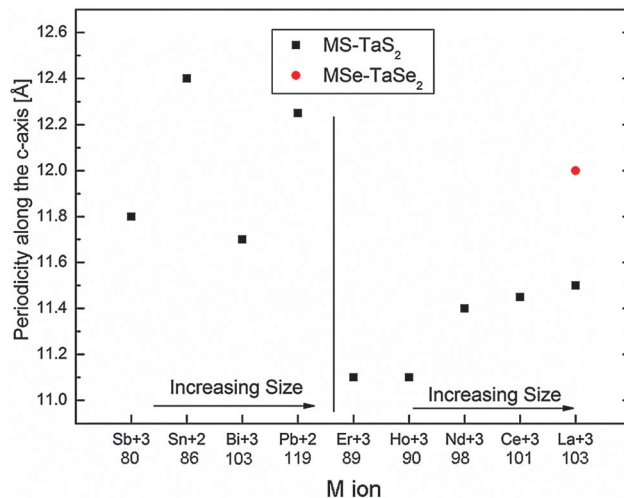


Fig. 6 Values of  $c$ -axis periodicity for tubular structures of MX-TX<sub>2</sub> MLC, presented schematically for the series of M atoms with increasing ionic radius shown in ascending order. The ionic radii of the M atoms in picometers are taken from Shannon–Prewitt Effective Ionic Radius at [http://www.knowledgedoor.com/2/elements\\_handbook/shannon-prewitt\\_effective\\_ionic\\_radius.html](http://www.knowledgedoor.com/2/elements_handbook/shannon-prewitt_effective_ionic_radius.html) and references thereof. Values for the MLC nanotubes with M = Sn, Pb, Sb and Bi are reproduced from data published previously<sup>7,18</sup> for comparison.

intermediate case.<sup>1,7,8,17,18</sup> Most of the Sb and Bi atoms in SbS and BiS are believed to be trivalent just as in their well known bulk compounds Sb<sub>2</sub>S<sub>3</sub> and Bi<sub>2</sub>S<sub>3</sub> respectively.<sup>19</sup> Strong charge transfer may result in a stronger electrostatic interaction between the LnS and TaS<sub>2</sub> layers, and consequently shorter bond lengths between the Ln and S atoms of the TaS<sub>2</sub> layer,<sup>8</sup> *i.e.*, smaller periodicity values along the  $c$ -axis (see Fig. 6).

Presumably, charge transfer between the two sublattices is responsible for the abundance of LnS-TaS<sub>2</sub> tubules that have a single folding vector in these samples. Despite the crystallographic equivalence of the 60° rotation of the LnS relative to the TaS<sub>2</sub> layer (see Fig. S1 in the ESI†), their orientations relative to the tubule axis are different. Obviously, only one (out of the three equivalent) common  $b$  axes between the LnS and TaS<sub>2</sub> of the LnS-TaS<sub>2</sub> slab can coincide with the nanotube axis (see Fig. S1 in the ESI†). Therefore, the  $b$ -axis of only one LnS layer (out of three) will coincide with the tubule axis. The energy associated with folding is believed to be minimal for the LnS layer, whose  $b$ -axis coincides with the tubule axis. Since the coupling between the layers is strong, it is believed that LnS-TaS<sub>2</sub> slabs without these rotational variants can be transformed more easily into nanotubes. This situation is obviously not the case for, *e.g.*, MS-TS<sub>2</sub> (M = Pb; T = Nb, Ta) tubules, in which the interlayer interaction is not as strong and tubules with three folding vectors for the MS layers and two folding vectors for the TS<sub>2</sub> layers are produced.<sup>7,14</sup>

Table 2 and Fig. 6 show that both the average interplanar periodicity along the  $c$ -axis corresponding to the LnS-TaS<sub>2</sub> (1 : 1) superstructure and the in-plane interplanar spacings decrease with increasing atomic number of Ln (*i.e.*, La, Ce, Nd, Ho, Er). Similar behavior was observed for bulk single crystals of LnS-TaS<sub>2</sub> MLC<sup>10</sup> and for tubular structures of MLC that are based on

$\text{LnS-CrS}_2$ .<sup>20</sup> This trend can be attributed to a decrease in the size of the  $\text{Ln}^{+3}$  ion with increasing atomic number. Similarly, the greater values of  $c$ -axis periodicity in  $\text{LaSe-TaSe}_2$ , when compared to that in isostructural  $\text{LaS-TaS}_2$ , can be attributed to the larger ionic radius of Se and the more covalent nature of its bonding with the metal atoms. For the sake of comparison, the interlayer spacing of nanotubes of the  $\text{MS-TaS}_2$  compounds with  $\text{M} = \text{Sb, Sn, Bi}$  and  $\text{Pb}$  are shown on the left side of the graph. Noticeably, the interlayer spacing of the MLC with stable  $\text{Sn}^{2+}$  and  $\text{Pb}^{2+}$  is larger than that of the MLC with  $\text{Sb}^{+3}$  and  $\text{Bi}^{+3}$  and the trivalent lanthanides. This observation suggests that the stability of the stable MLC with  $\text{M}^{+3}$  is attained by a significant degree of charge transfer from the metal  $\text{M}$  to the Ta atom.

## Electronic structure

The density-functional tight-binding (DFTB)<sup>21,22</sup> method was used to calculate the electronic structure of bulk  $\text{LaS-TaS}_2$  as shown in Fig. 7. (The electronic structures obtained by the

DFTB method are comparable to the full density functional theory (DFT) method as shown in Fig. S9 (ESI†). Therefore the use of the DFTB method for the calculations is justified.) The electronic structure including local densities of states, atom-resolved charges and the resulting charge transfer of this specific family of MLC were not reported before. Since the lattice structure is incommensurate along the  $a$ -direction ( $a_{\text{LaS}}/a_{\text{TaS}_2}$  is an irrational number), a supercell approximation which is identical to that of previous publications,<sup>23</sup> *i.e.*  $4 \times a_{\text{LaS}} \approx 7 \times a_{\text{TaS}_2}$  was used. This cell (see Fig. 7a) contains four sublayers (2 LaS and 2 TaS<sub>2</sub>) due to the fact, that this compound forms a so called CF structure (see Fig. 4 in ref. S7) with an inversion center between the two TaS<sub>2</sub> sublayers.

From the isolated LaS and TaS<sub>2</sub> sublayers, one would expect electron transfer from La to Ta in the combined system (see the DOS curves of LaS and TaS<sub>2</sub> in Fig. S10 in the ESI†). The calculated DOS of the LaS-TaS<sub>2</sub> compound is shown in Fig. 7b–e (solid black curve). An analysis of the integrated local density of states (LDOS) as well as a Mulliken population analysis show an increase of the electron density on the Ta

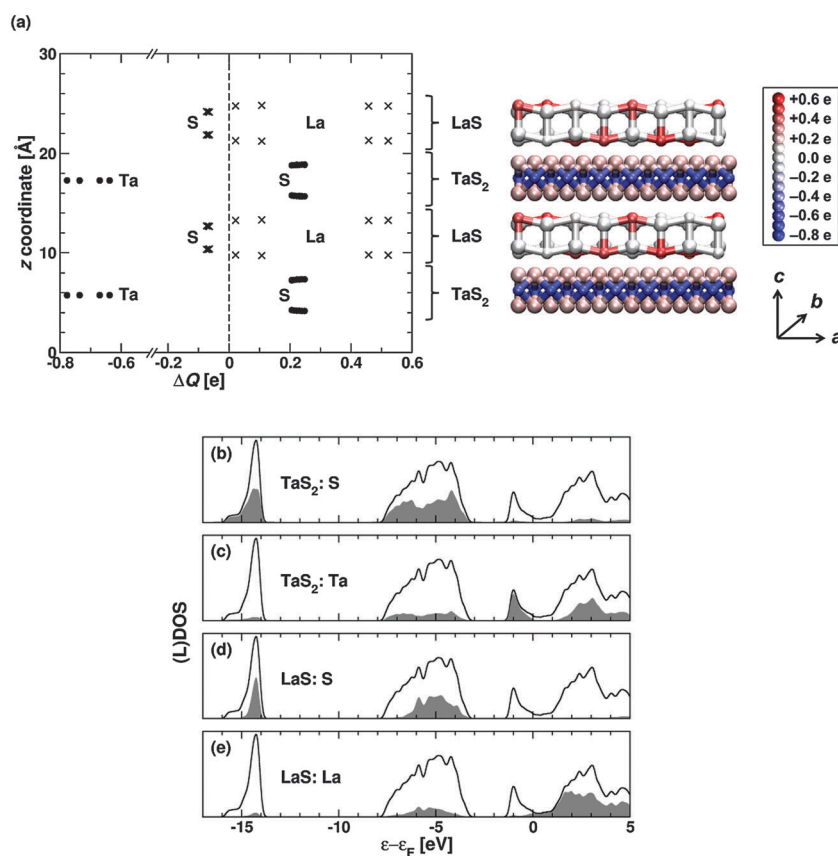


**Fig. 7** (a) The changes in the atomic charges ( $\Delta Q$ ) of the atoms in the compound, compared to the charges of the atoms of the isolated LaS and TaS<sub>2</sub> layers. The structure is shown in a view along the normal to the (020) plane of a LaS-TaS<sub>2</sub> unit cell (labeled according to the ortho-pseudohexagonal system for TaS<sub>2</sub>). The individual atoms are colored according to the  $\Delta Q$  values in the left diagram with a color code shown on the right side. The “-” and “+” signs represent gained and donated (depleted) electronic charges, respectively. The La atoms (small spheres) are shown in different hues of gray to pink, depending on their positions relative to the TaS<sub>2</sub> sublayer and subsequent  $\Delta Q$ . The Ta atoms (small spheres) are colored in blue and the S (large spheres) atoms in pink in the TaS<sub>2</sub> sublayer and in grey in the LaS sublayer. (b–e) Show the total and local density of states for the LaS-TaS<sub>2</sub> compound. The solid black lines correspond to total DOS curves. The local densities of states of the atom types are shown in grey: (b) S atoms and (c) Ta atoms in the TaS<sub>2</sub> sublayer, (d) S atoms and (e) La atoms in the LaS sublattice. The energy is given relative to the Fermi energy of the LaS-TaS<sub>2</sub> compound.

atoms and a decrease of the electron density on the La atoms in the LaS–TaS<sub>2</sub> system compared to the isolated LaS/TaS<sub>2</sub> layers. Different values of the transferred charges  $\Delta Q$  (relative to their charges in the pristine LaS and TaS<sub>2</sub> layers) were obtained for the different La atoms (see Fig. 7a). This results from the different lattices of the subsystems and consequently from different positions of the La atoms relative to the atoms in the TaS<sub>2</sub> sublayers. The variation in charge transfer to the Ta atoms in the unit cell is much smaller (see Fig. 7a) due to the shielding of the Ta atoms by the sulfur atoms. The smallest spreading of the charge transfer was found for the sulfur atoms within the two sublayers. On average every La atom has lost 0.28 electrons, while every Ta atom has gained 0.69 electrons, compared to the isolated monolayers (see Fig. 7a and Table S2 in the ESI†). *I.e.* the electron transfer from the La d-states to the Ta d-states is compensated to some extent by corresponding changes in the S charges in each subsystem (see Table S2, ESI†) which is opposed in sign relative to the metal atoms.

Consequently, a relatively small net electron transfer between the TaS<sub>2</sub> and LaS layers ( $\sim 0.2$  electrons per formula unit) occurs. The charge transfer from the La to the Ta atom is dominated by the states near the Fermi level and results in a filled  $d_{2z}$  band of the Ta atoms in the combined system (Fig. 7c). Whereas both isolated monolayers have pronounced metallic character (Fig. S10, ESI†), the LaS–TaS<sub>2</sub> compound has an overall semi-metallic behavior, in which the TaS<sub>2</sub> layers are almost semi-metallic and the LaS layers are effectively nonmetallic. A more detailed discussion of the electronic structure will be given in a separate publication.

## Raman spectroscopy

Raman spectroscopy measurements were carried-out on single LaS–TaS<sub>2</sub> and NdS–TaS<sub>2</sub> tubular crystals of 200–500 nm thickness (see Fig. 8). The differences between the Raman modes of pristine bulk LnS<sup>24</sup> and 2H–TaS<sub>2</sub><sup>25</sup> and the modes observed in the corresponding MLC can be interpreted in terms of charge

transfer from the LnS to the TaS<sub>2</sub> layers.<sup>25</sup> Charge transfer increases both the intralayer and the interlayer interaction between the layers, thereby affecting the Raman frequencies. In addition, the Raman spectra are expected to be affected by the mutual structural modulation. Recall that the structure of the LnS layers (and to a lesser extent that of the TaS<sub>2</sub> layers) within the MLC is slightly different from bulk LnS with a NaCl structure.

Representative Raman spectra recorded from single tubular nanocrystals of LaS–TaS<sub>2</sub> and NdS–TaS<sub>2</sub> are shown in Fig. 8. A spectrum of a 2H–TaS<sub>2</sub> platelet was measured for comparison as well. The spectra recorded from LaS–TaS<sub>2</sub> MLC tubular crystals are in excellent agreement with the results published previously for a bulk single crystal of LaS–TaS<sub>2</sub> MLC.<sup>25</sup>

The mode at 400 cm<sup>-1</sup> is in perfect agreement with the A<sub>1g</sub> (intralayer out-of-plane vibration) mode of 2H–TaS<sub>2</sub>.<sup>25</sup> The mode at 327 cm<sup>-1</sup> is attributed to the E<sub>2g</sub> (intralayer in-plane vibration) mode, which occurs at 286 cm<sup>-1</sup> in bulk 2H–TaS<sub>2</sub>.<sup>25</sup> The large upshift of the intralayer E<sub>2g</sub> mode of the TaS<sub>2</sub> (41 cm<sup>-1</sup> in this case) has been reported for various intercalation compounds of 2H–TaS<sub>2</sub> (and 2H–NbS<sub>2</sub>), including the misfit compounds<sup>25–27</sup> and is attributed to charge transfer from the LnS to the TaS<sub>2</sub> layers. The mode at  $\sim 149$  cm<sup>-1</sup> matches the A<sub>1g</sub> (intralayer out-of-plane vibration) mode at 148 cm<sup>-1</sup> of LaS in a LaS–TaS<sub>2</sub> MLC single crystal. An additional A<sub>1g</sub> mode at 122 cm<sup>-1</sup> was observed by Kisoda *et al.*<sup>25</sup> but was not observed here due to experimental limitations at lower wavenumbers. As mentioned previously, the observed Raman modes of the LaS layers within LaS–TaS<sub>2</sub> MLC are different from the modes observed in LaS bulk single crystals with NaCl structure.<sup>24</sup> The broad band between  $\sim 240$  and 303 cm<sup>-1</sup> is attributed to the two-phonon band as detailed elsewhere.<sup>25</sup>

The spectra recorded from NdS–TaS<sub>2</sub> tubular crystals are quite similar to their LaS–TaS<sub>2</sub> counterparts. However, no previous literature data could be found for bulk NdS–TaS<sub>2</sub> MLC. Inasmuch as spectra recorded from bulk LnS–TaS<sub>2</sub> MLC with (Ln = La, Ce, Sm and Gd) were found to be similar,<sup>25</sup> the similarity of NdS–TaS<sub>2</sub> is not surprising.

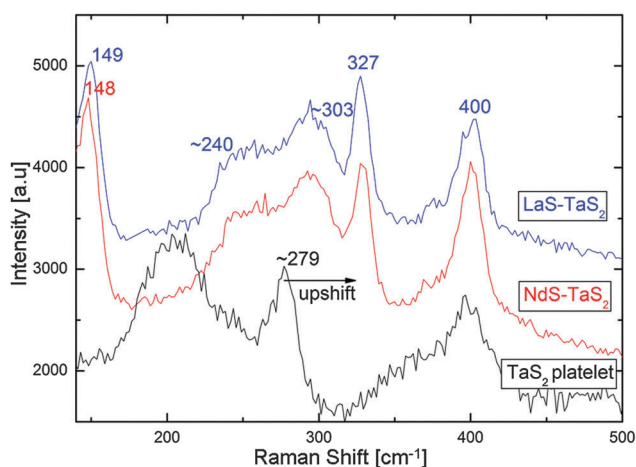


Fig. 8 Raman spectra of single LaS–TaS<sub>2</sub> and NdS–TaS<sub>2</sub> tubular crystals. A spectrum recorded from a TaS<sub>2</sub> platelet is also shown for comparison.

## Conclusions

Nanotubular structures were formed from LnS–TaS<sub>2</sub> (Ln = La, Ce, Nd, Ho, Er) and LaSe–TaSe<sub>2</sub> MLC in evacuated silica tubes when subjected to appropriate temperature profiles and growth times. The compounds were found to be commensurate along the *b*-axis and incommensurate along the *a*-axis. SAED patterns of the tubes suggest a single folding vector for the LnS(Se) and TaS<sub>2</sub>(Se) layers in many cases. As expected, the commensurate *b*-axes of the LnS(Se) and TaS<sub>2</sub>(Se) layers coincide with the tubule axis.

The mutual structural modulation of the TaS<sub>2</sub>(Se) and LnS(Se) lattices results in an orthorhombic distortion of the rocksalt LnS(Se) lattice, while the TaS<sub>2</sub>(Se) is barely modified. The difference between the in-plane lattice parameters (*a* and *b*) of LnS in LnS–TaS<sub>2</sub> MLC became more significant for HoS and

ErS than for LaS, LaSe, CeS and NdS. Both the *c*-axis periodicity of the LnS–TaS<sub>2</sub> superstructure and the in-plane lattice periodicities of the LnS and TaS<sub>2</sub> layers decrease with increasing atomic number of Ln. The periodicity is greater for selenides than for corresponding sulfides.

The smaller periodicities in the LnS–TaS<sub>2</sub> tubules relative to their SnS–TaS<sub>2</sub> and PbS–TaS<sub>2</sub> counterparts indicate a stronger interaction between the two subsystems for the former. Such an observation is supported by a high upshift in the E<sub>2g</sub> Raman mode of TaS<sub>2</sub> in these compounds. Theoretical calculations for LaS–TaS<sub>2</sub> indicate a small net charge transfer from the LaS layer to the hexagonal sublattice. But on the other hand, also larger changes of the metal atom's charges and consequently of the occupations of their electronic states can be observed. This results in a nearly full occupied d<sub>z<sup>2</sup></sub> band in the TaS<sub>2</sub> subsystem. Hence, the electronic structure of the TaS<sub>2</sub> part is comparable to that of MoS<sub>2</sub> or WS<sub>2</sub>.

## Competing financial interest

The authors declare no competing financial interest.

## Acknowledgements

RT acknowledges the support of the Israel Science Foundation; German-Israeli Foundation (GIF); The FTA action of the Israel National Nano-Initiative; the H. Perlman Foundation; the G. M. J. Schmidt Minerva Center for Supramolecular Chemistry; the Irving and Azelle Waltcher Foundations in honor of Prof. M. Levy and the Irving and Cherna Moskowitz Center for Nano and Bio-Nano Imaging. GS, JOJ and TL would like to acknowledge the financial support of the DFG (ICENAP project), for computational time provided by ZIH Dresden (project QDSIM) and for helpful discussions with I. Baburin, K. Trepte and D. Lenz.

## References

- 1 G. A. Wiegers, *Prog. Solid State Chem.*, 1996, **24**, 1–139.
- 2 G. A. Wiegers and A. J. Meerschaut, *J. Alloys Compd.*, 1992, **178**, 351–368.
- 3 F. Jelinek, *J. Less-Common Met.*, 1962, **4**, 9–16.
- 4 A. H. Thompson, R. F. Gamble and J. F. Revelli, *Solid State Commun.*, 1971, **9**, 981–985.
- 5 J. F. Revelli, *Inorg. Synth.*, 1979, **19**, 35–49.
- 6 A. Meetsma, G. A. Wiegers, R. J. Haange and J. L. de Boer, *Acta Crystallogr., Sect. C: Cryst. Struct. Commun.*, 1990, **46**, 1598–1599.
- 7 G. Radovsky, R. Popovitz-Biro and R. Tenne, *Chem. Mater.*, 2014, **26**, 3757–3770.
- 8 G. A. Wiegers, *J. Alloys Compd.*, 1995, **219**, 152–156.
- 9 F. J. Di-Salvo, G. W. Hull, L. H. Schwartz, J. M. Voorhoeve and J. V. Waszczak, *J. Chem. Phys.*, 1973, **59**, 1922–1929.
- 10 K. Suzuki, T. Enoki and K. Imaeda, *Solid State Commun.*, 1991, **78**, 73–77.
- 11 D. Reefman, J. Baak, H. B. Brom and G. A. Wiegers, *Solid State Commun.*, 1990, **75**, 47–51.
- 12 N. Katayama, M. Nohara and H. Tagaki, *Phys. C*, 2006, **445**, 35–38.
- 13 D. Bernaerts, S. Amelinckx, G. van Tendeloo and J. van Landuyt, *J. Cryst. Growth*, 1997, **172**, 433–439.
- 14 G. Radovsky, R. Popovitz-Biro, D. G. Stroppa, L. Houben and R. Tenne, *Acc. Chem. Res.*, 2014, **47**, 406–416.
- 15 J. L. de Boer, A. Meetsma, T. J. Zeinstra, R. J. Haange and G. A. Wiegers, *Acta Crystallogr., Sect. C: Cryst. Struct. Commun.*, 1991, **C47**, 924–930.
- 16 S. Kuypers, J. van Landuyt and S. Amelinckx, *J. Solid State Chem.*, 1990, **86**, 212–232.
- 17 G. A. Wiegers, *Jpn. J. Appl. Phys.*, 1993, **32**, 705–710.
- 18 L. S. Panchakarla, G. Radovsky, L. Houben, R. Popovitz-Biro, R. E. Dunin-Borkowski and R. Tenne, *J. Phys. Chem. Lett.*, 2014, **5**, 3724–3736.
- 19 Y. Ren, C. Haas and G. A. Wiegers, *J. Phys.: Condens. Matter*, 1995, **7**, 5949–5958.
- 20 L. S. Panchakarla, R. Popovitz-Biro, L. Houben, R. E. Dunin-Borkowski and R. Tenne, *Angew. Chem., Int. Ed.*, 2014, **53**, 6920–6924.
- 21 D. Porezag, T. Frauenheim, T. Köhler, G. Seifert and R. Kaschner, *Phys. Rev. B: Condens. Matter Mater. Phys.*, 1995, **51**, 12947–12957.
- 22 G. Seifert, D. Porezag and T. Frauenheim, *Int. J. Quantum Chem.*, 1996, **58**, 185–192.
- 23 C. M. Fang, S. van Smaalen, G. A. Wiegers, C. Haas and R. A. de Groot, *J. Phys.: Condens. Matter*, 1996, **8**, 5367–5382.
- 24 I. Morke, E. Kaldis and P. Wachter, *Phys. Rev. B: Condens. Matter Mater. Phys.*, 1986, **33**, 3392–3398.
- 25 K. Kisoda, M. Hangyo, S. Nakashima, K. Suzuki, T. Enoki and Y. Ohno, *J. Phys.: Condens. Matter*, 1995, **7**, 5383–5393.
- 26 M. Hangyo, K. Kisoda, S. Nakashima, A. Meerschaut and J. Rouxel, *Phys. B*, 1996, **219–220**, 481–483.
- 27 M. Hangyo, K. Kisoda, T. Nishio, S. Nakashima, T. Terashima and N. Kojima, *Phys. Rev. B: Condens. Matter Mater. Phys.*, 1994, **50**, 12033–12043.